ACS APPLIED MATERIALS & INTERFACES

Research Article

www.acsami.org

In-Depth Understanding of the Morphology–Performance Relationship in Polymer Solar Cells

Wenchao Huang,[†] Eliot Gann,[†,‡] Yi-Bing Cheng,*[,†] and Christopher R. McNeill*[,†]

[†]Department of Materials Science and Engineering, Monash University, Melbourne, Victoria 3800, Australia

[‡]Australian Synchrotron, 800 Blackburn Road, Melbourne, Victoria 3168, Australia

Supporting Information

ABSTRACT: It is well-established that thermal annealing optimizes the morphology and improves the efficiency of P3HT-based organic solar cells, but the effects of different cooling rates after annealing are not well understood. In this paper, we use a model system based on poly(3-hexylthiophene) (P3HT) and phenyl-C_{61}-butyric acid methyl ester (PCBM) to examine the relationship between morphology and device performance for annealing before (preannealing) and after (postannealing) the application of the electrode, with different cooling rates and in different device architectures. In the conventional structure, postannealing is confirmed to significantly enhance efficiency. The device prepared with a slow cooling rate (3.6%) shows a higher average power conversion efficiency than that prepared with a fast cooling rate (3.3%). The microstructural changes underlying this 10% increase in device performance and further effects of cooling rate, pre- and postannealing, and device architecture are comprehensively examined with a combination of synchrotron-based techniques, including grazing incidence wide-angle X-ray scattering, near-edge X-ray absorption fine structure spectroscopy, and X-ray photoelectron spectroscopy. The best device in the conventional architecture (postannealed with slow cooling rate) shows a more face-on orientation and narrower orientational distribution of P3HT crystallites. In addition, postannealing leads to PCBM diffusion toward the blend/top electrode interface. The enrichment of PCBM at the blend/top electrode interface plays a positive role in aiding electron collection at the electrode in the conventional structure, but it has a negative effect on the performance of the inverted structure, where hole collection at the top electrode instead is required. For this reason, in an inverted structure, preannealed films with slow cooling exhibit the best photovoltaic performance.

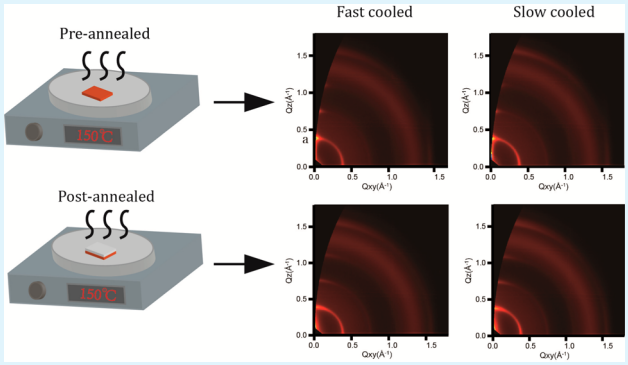

KEYWORDS: *organic solar cells, thermal annealing, cooling rates, grazing incident wide-angle X-ray scattering, near-edge X-ray absorption fine structure spectroscopy*

INTRODUCTION

Organic photovoltaics have attracted a great deal of interest over the past two decades due to their low cost and scalable solution processability.[1,2] Solution processing provides the possibility of fabricating organic devices on flexible substrates and over large areas. Since the invention of the bulk heterojunction (BHJ) in 1995,[3,4] the power conversion efficiency of polymer solar cells has experienced a dramatic increase approaching 11% recently.[5−7] BHJs consisting of interpenetrating networks of electron donor and electron acceptor provide a large interfacial area where efficient exciton dissociation can occur. The control of this morphology and molecular packing play an important role in obtaining high-efficiency organic photovoltaic devices.[8−10] Various processing techniques have been employed to improve and optimize BHJ morphologies for achieving high efficiencies, including thermal annealing,[8,11−14] solvent annealing,[15−17] and the introduction of solvent additives.[18−20]

Among the various treatments, thermal annealing is a successful process for optimizing the morphology of poly(3-hexylthiophene) (P3HT)-based devices. In 2003, Padinger et al. reported that thermal annealing led to a dramatic increase in the performance of solar cells based on P3HT and phenyl-C_{61}-butyric acid methyl ester (PCBM), with the efficiency increasing from 0.4% to over 2.5%.[21] Chirvase et al. suggested that the increased efficiency of annealed organic solar cells is a result of the enhancement of the optical absorption of P3HT and the diffusion of PCBM out of the P3HT phase to form separated clusters.[22] Ma and co-workers achieved a solar cell efficiency approaching 5% by using a postannealed P3HT/PCBM blend.[11] This advancement in device efficiency is explained by thermally induced crystallization of P3HT and improved contact between the polymer blend and the charge-

Received: April 12, 2015
Accepted: May 28, 2015
Published: May 28, 2015

DOI: 10.1021/acsami.5b03095
ACS Appl. Mater. Interfaces 2015, 7, 14026−14034

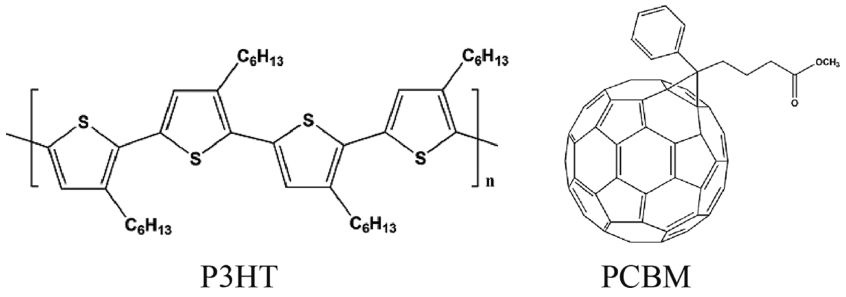

Figure 1. Chemical structures of P3HT and PCBM.

collecting electrodes. To understand the morphological changes upon thermal annealing, ex situ and in situ scattering techniques combined with transmission microscopies have been widely used to examine the crystallization behavior of the blend at elevated temperature.[13,23,24] Elevated temperature allows polymer reorganization into fibrillar crystallites creating microphase separation and highly ordered interpenetrating networks.[13,23,25,26] Polymer reorganization and proper phase separation have been considered to be the main reason for the improvement of device performance after thermal treatment.

Although the underlying cause of this efficiency improvement upon thermal annealing has attracted extensive studies,[8,23,27−31] the influence of different cooling rates on solar cells performance remains largely unexplored, particularly for postannealed samples. In this paper, we use the model P3HT/PCBM system (chemical structures are shown in Figure 1) to demonstrate that the cooling rate significantly affects photovoltaic performance. The morphological changes behind device performance are investigated by synchrotron-based X-ray techniques. Grazing incidence wide-angle X-ray scattering (GIWAXS) is a reciprocal-space technique which provides information regarding molecular packing, such as lattice spacings, coherence lengths and the orientation of crystalline planes. Face-on stacking of the polymer (with side-chain stacking parallel to the substrate and the molecular face−face π-stacking perpendicular to the substrate) is the preferential orientation for hole transport across the active layer because of the anisotropic charge-transport properties of P3HT.[32]

In addition to the lateral morphology, vertical stratification and enrichment at the organic−metal interface is directly linked to the charge extraction efficiency and recombination.[14,31,33] In a previous study, Xue and co-workers have found that there is a P3HT capping layer at an air/polymer interface after spin coating.[34] They also compared the interfacial structural change upon different cooling rates. However, all samples that they measured were preannealed (without the Al electrode). During device fabrication, thermal annealing with the Al electrode in place is necessary to achieve high-efficiency P3HT/PCBM solar cells in the conventional structure. Here, the combination of near-edge X-ray absorption fine structure (NEXAFS) and X-ray photoelectron spectroscopy (XPS) were used to monitor the interfacial structure after postannealing for different cooling rates. NEXAFS and XPS are, due to the short mean free path of photoelectrons, surface-sensitive techniques and are effective tools to quantitatively measure the chemical composition information at the blend interface. NEXAFS in particular is sensitive to the molecular composition and orientation at the surface of a blend. By detecting the electron yield intensity as a function of X-ray angles of incidence, we can determine both the composition and average tilt angle at the surface of a blend. In this work, we use GIWAXS, NEXAFS, and XPS together to uncover the morphological changes that occur upon pre- and postannealing with different cooling rates. Understanding the structural change from molecular to mesoscopic scales upon different cooling rates plays an important role in further optimizing the efficiency of organic solar cells.

METHODOLOGY

Materials. P3HT was supplied by Rieke Metals (4002-E; Lincoln, NE) with a molecular weight (M_W) of 51 000 g/mol and a dispersity of 2.4. PCBM was purchased from Nano-C (Westwood, MA).

Device Fabrication. All conventional architecture devices were constructed with a structure of ITO/PEDOT:PSS/P3HT:PCBM/Al [ITO, indium tin oxide; PEDOT, poly(3,4-ethylenedioxythiophene); PSS, poly(styrenesulfonate)]. The active layer was spin-coated on patterned ITO glass covered with a layer of PEDOT:PSS (Baytron P VP AI 4-83; Heraeus Precious Metals GmbH & Co. KG, Leverkusen Germany). PEDOT:PSS was first spin-coated on the precleaned ITO glass with 5000 rpm for 45 s before being introduced into a nitrogen glovebox. The PEDOT:PSS-coated substrates were annealed for 15 min at 120 °C. P3HT and PCBM were dissolved in anhydrous dichlorobenzene at concentrations of 15 mg/mL for P3HT and 15 mg/mL for PCBM. The blend solution was spin-coated at 1200 rpm for 60 s prior to the evaporation of Al. The inverted-architecture devices were based on the structure of ITO/PEIE/P3HT:PCBM/MoO_3/Ag (PEIE, polyethylenimine ethoxylate). PEIE (0.4 wt % in methoxyethanol) was spin-coated on the ITO glass, followed by thermal annealing at 110 °C for 10 min. The active layers were prepared with the same process in conventional structure. Molybdenum oxide and silver were consecutively thermally evaporated with thicknesses of 15 and 100 nm, respectively. The devices were thermally annealed at 150 °C for 10 min before (preannealing) or after (postannealing) the top electrode was applied with different cooling rates. For the fast-cooling and medium-cooling processes, the samples were transferred to a piece of metal (with a couple of sheets of paper on top for the medium rate) after thermal treatment, while for the slow-cooling process, the hot plate was switched off and the samples remained on the hot plate until it reached room temperature. The temperature as a function of cooling time with different cooling rates was measured by a thermal couple; see Figure S1.

Device Characterization. The power conversion efficiencies of solar cells were measured under 1 sun AM 1.5G with a Photo Emission Tech model SS50AAA solar simulator with the current−voltage curves collected using a Keithley 2635 source meter. The light intensity was set by a calibrated silicon photodiode. External quantum efficiency (EQE) was measured as a function of wavelength by dispersing light from a tungsten filament. The light was split by a monochromator (Oriel Cornerstone 130) with the intensity of less than 1 mW cm^{-2} in a spot size smaller than the device active area. The short-circuit current was recorded by a Keithley 2635 source meter.

Microstructure Characterization. The samples for ultraviolet−visible light spectroscopy (UV−vis) characterization were spin-coated on quartz substrates. The absorption spectra of all samples were collected with a Lambda 950 spectrophotometer from PerkinElmer.

DOI: 10.1021/acsami.5b03095
ACS Appl. Mater. Interfaces 2015, 7, 14026−14034

GIWAXS experiments were conducted at the Australian Synchrotron on the SAXS/WAXS beamline.[35] All the samples were deposited on silicon wafers following the same procedure as device fabrication. For the postannealed blend, the evaporated cathodes were removed by a 0.1 M sodium hydroxide solution before X-ray experiments. Samples were irradiated by 9 keV X-rays at a fixed incident angle of 0.16° and the two-dimensional (2D) scattering patterns were recorded by a Dectris Pilatus 1 M detector. The incident angle of X-ray was close to the critical angle of the polymer film but below the critical angle of the silicon wafer, minimizing the background signal from the substrate. The X-ray exposure time was 3 s such that no film damage was identified. The results were analyzed by an altered version of the NIKA 2D based on Igor Pro software.[36,37]

NEXAFS spectra were measured at the soft X-ray (SXR) beamline at the Australian Synchrotron. The carbon edge spectra were collected in a scan from 280 to 320 eV.[38] Total electron yield (TEY) spectra were measured by recording the drain current flowing to the sample. Spectra were normalized by the "stable monitor method", followed by background subtraction and then normalized to 1 at 320 eV and 0 at 280 eV, similar to previous studies.[39,40] XPS measurements were also conducted at the SXR beamline with an X-ray energy of 1486.7 eV with photoelectrons being detected using a SPECS Phoibos 150 Hemispherical Analyzer with a pass energy of 40 eV.

RESULTS AND DISCUSSION

Normalized UV−vis spectra are shown in Figure 2. The UV−vis spectra show a significant change after thermal annealing,

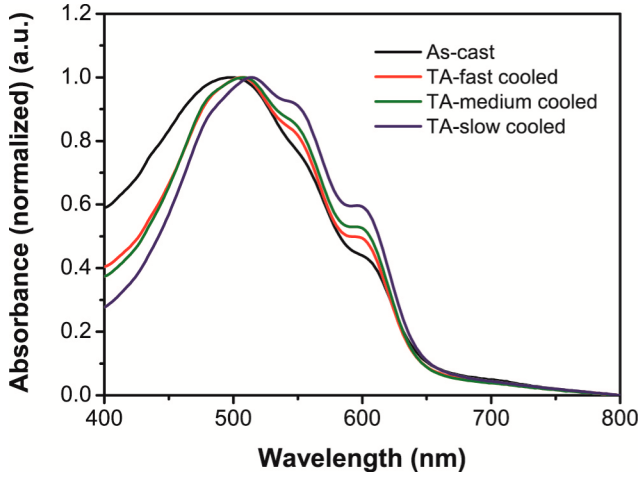

Figure 2. Normalized UV−vis spectra of as-casted and thermally annealed P3HT/PCBM blend with different cooling rates.

with a significant red shift observed with thermal annealing. In addition, the intensity of the vibronic shoulder at 610 nm shows a systematic increase from fast cooling (red line) to slow cooling (blue line). This vibronic shoulder is related to the 0−0 vibronic transition; hence, its intensity is related to the degree of interchain order.[41,42] The highest vibronic intensity is observed in the slow-cooled blend, indicating that slow cooling favors polymer reorganization into a highly ordered structure, which plays an important role for charge transport through the polymer.

Photovoltaic performance of the conventional structure P3HT/PCBM solar cell is presented in Figure 3. Compared with the as-cast device, both preannealed and postannealed devices show improved efficiencies. However, the postannealed sample shows a better photovoltaic performance than the preannealed sample. In particular, the postannealed sample (medium-cooled) shows a higher open-circuit voltage, short-

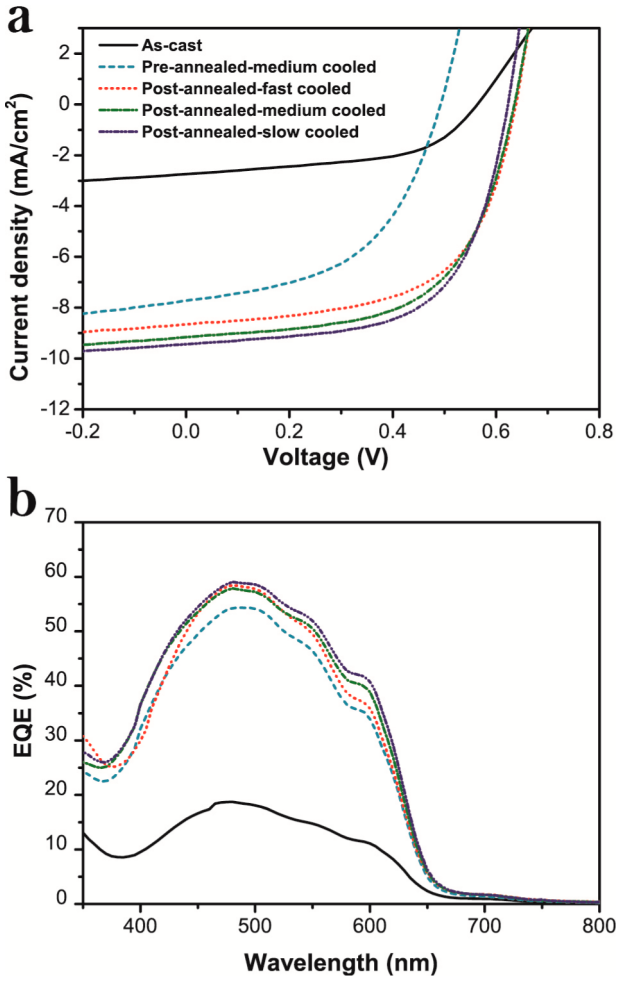

Figure 3. Device performance of conventional P3HT/PCBM solar cells with different cooling rates. (a) Current density versus voltage curve under AM 1.5 G illumination. (b) External quantum efficiency spectra.

circuit current, fill factor, and efficiency with values of 0.63 V, 9.16 mA/cm^2, 0.60, and 3.44%, respectively, compared to the preannealed device (medium-cooled) with values of 0.49 V, 7.72 mA/cm^2, 0.51, and 1.94%, respectively.

Figure 3a also plots an evolution of postannealed device performance as a function of cooling rates with the detailed parameters summarized in Table 1 (Preannealed device performance as a function of cooling rates is shown in Figure S2 and the detailed parameters are presented in Table S1). Device performance is closely linked to cooling rate. Among the postannealed samples, the sample with the slowest cooling rate exhibits the best performance with a power conversion

Table 1. Photovoltaic Performance of Conventional P3HT/PCBM Solar Cells

	cooling rates	V_{oc} (V)	J_{sc} (mA/cm^2)	FF	efficiency (%)
as-cast		0.56	2.74	0.53	0.82 (±0.27)
preannealed	medium-cooled	0.49	7.72	0.51	1.94 (±0.21)
postannealed	fast-cooled	0.64	8.66	0.59	3.27 (±0.13)
postannealed	medium-cooled	0.63	9.16	0.60	3.44 (±0.15)
postannealed	slow-cooled	0.62	9.44	0.62	3.63 (±0.18)

DOI: 10.1021/acsami.5b03095
ACS Appl. Mater. Interfaces 2015, 7, 14026−14034

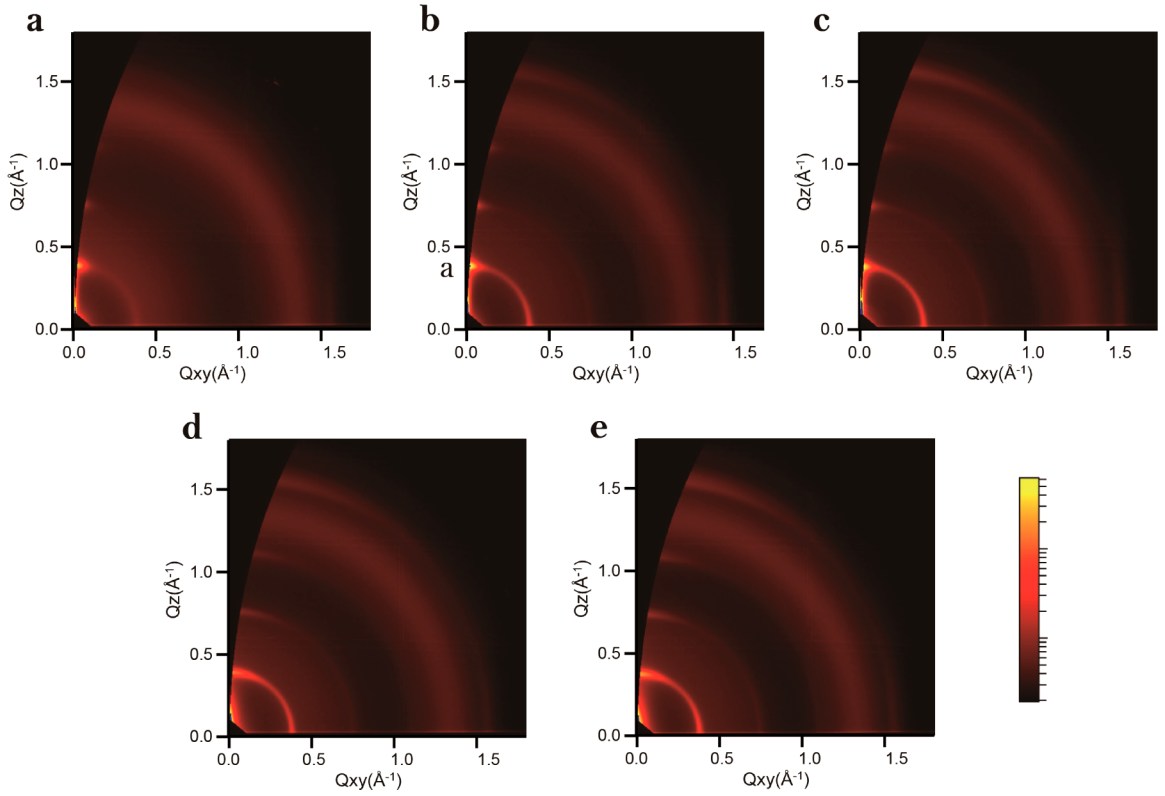

Figure 4. 2D GIWAXS images of P3HT/PCBM films (a) as-cast, (b) preannealed with fast-cooling rate, (c) preannealed with slow-cooling rate, (d) postannealed with fast-cooling rate, and (e) postannealed with slow-cooling rate.

efficiency of 3.63% and short-circuit current of 9.44 mA/cm^2, while in the fast-cooled sample, the efficiency and short-circuit current are only 3.27% and 8.66 mA/cm^2, respectively. A similar trend with the short-circuit current increasing with the decreased cooling rates is also observed in the low light intensity EQE measurements (Figure 3b), which shows a good agreement in the short-circuit current measured under the solar simulator.

Figure 4 shows the 2D GIWAXS patterns collected from films with different annealing conditions and different cooling rates. In the as-cast sample, several diffraction peaks are apparent along the out-of-plane (vertical) direction. The diffraction peaks located at momentum transfers out of plane (q_z) of 0.38, 0.75, and 1.12 Å^{-1} correspond to (100), (200), and (300) reflections, indicating that P3HT is predominately stacking in an edge-on structure with the side-chain stacking direction perpendicular to the substrate. In the thermally annealed sample, the scattered intensity of the (100) peak is significantly increased and a new diffraction peak is observed at q_z = 1.58 Å^{-1}, corresponding to π-stacking (020) peaks indicating the existence of crystallites with face-on orientation.

For further study of the microstructure of P3HT, line profiles taken from the diffraction patterns along the out-of-plane and in-plane directions are plotted in Figure 5. The *d*-spacing of each peak corresponds to the peak position, while the coherence length of the corresponding crystalline axis is indicated by the full width at half-maximum (fwhm). The peak parameters are summarized in Table S2. The *d*-spacing of the (100) crystalline axis is 1.65 nm in all samples, regardless of annealing conditions. However, a significant increase in coherence length is observed upon annealing. The coherence length of the out-of-plane (100) peaks increases from 14.6 nm in the as-cast film to 19.6 nm in preannealed film (fast-cooled) and to 20.9 nm in postannealed film (fast-cooled). Compared to the quickly cooled samples, films cooled slowly exhibit slightly lower coherence lengths of 18.5 nm (preannealed) and 20.3 nm (postannealed) in the out-of-plane (100) peak. However, a more prominent out-of-plane π-stacking (020) peak and increase in the coherence length and intensity of the in-plane (IP) (100) peak are observed (an IP (100) peak corresponds to face-on crystallites). The coherence length of the IP (100) peak increases from 20.3 nm (fast-cooled) to 21.7 nm (slow-cooled) in the preannealed sample, and from 21.7 nm (fast-cooled) to 22.4 nm (slow-cooled) in the postannealed sample. Thus, a more face-on structure with π-stacking perpendicular to the substrate emerges with a slower cooling rate which likely facilitates charge transport in the vertical direction, the direction charge carriers must migrate to reach the electrodes.[43] The reason why a slow-cooling rate seems to promote a face-on configuration compared to fast cooling, however, is not clear and would require further investigation.

When the effects of pre- and postannealing are compared, there is a negligible difference in peak position (crystalline spacing). However, as shown in Figure 4, a broader orientational distribution of the OOP (100) peak is found in the postannealed scattering pattern due to the presence of the Al electrode, indicating that the edge-on stacking behavior is less well-oriented. Figure 6 shows the partial pole figure of the (100) peak cut from 2D GIWAXS images. Note that polar angles lower than the scattering angles are impossible to record in the grazing angle geometry. All peaks are fit by a Gaussian function and the fwhm's are summarized in Table 2. The preannealed sample exhibits a polymer orientation similar to the as-cast sample. However, the FWHM of postannealed OOP

DOI: 10.1021/acsami.5b03095
ACS Appl. Mater. Interfaces 2015, 7, 14026−14034

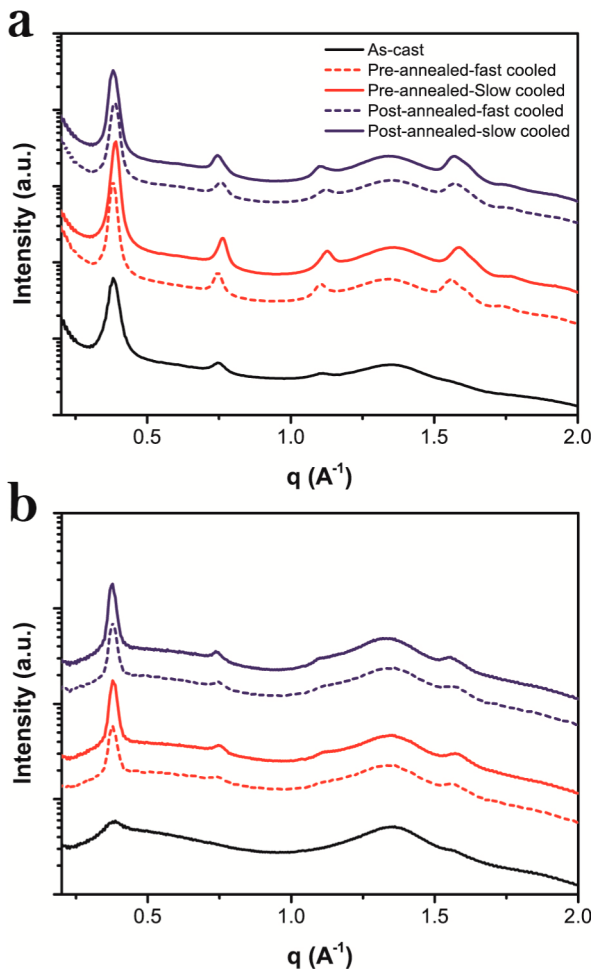

Figure 5. Line profiles taken from the 2D GIWAXS patterns: (a) out-of-plane direction (OOP); (b) in-plane direction (IP).

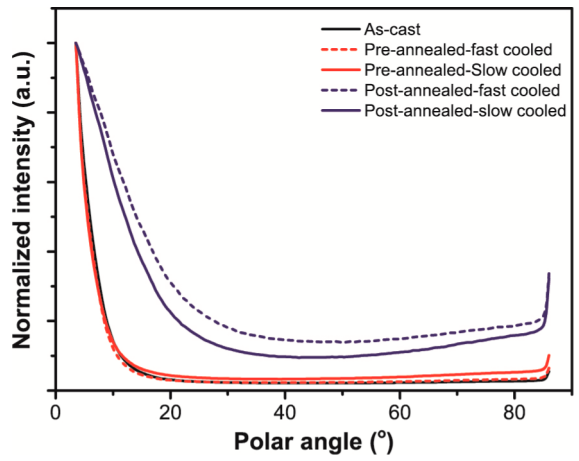

Figure 6. Pole figure of the (100) reflection of P3HT in the blend film.

(100) peak exhibits a significant increase, from 10.4° in as-cast film to 24.8° in postannealed film with fast cooling. When comparing the postannealed blend with different cooling rates, better-oriented edge-on P3HT crystallites are seen in the slow-cooled blend film with a FWHM value of 21.6°.

Figure 7a shows the carbon K-edge NEXAFS spectra of films with different annealing conditions, which were used to determine surface composition. NEXAFS spectra have been

Table 2. Fitted Value of FWHM from the Pole Figure of the (100) Peak

	cooling rate	fwhm (deg)
as-cast		10.4
preannealed	fast	9.7
preannealed	slow	9.6
postannealed	fast	24.8
postannealed	slow	21.6

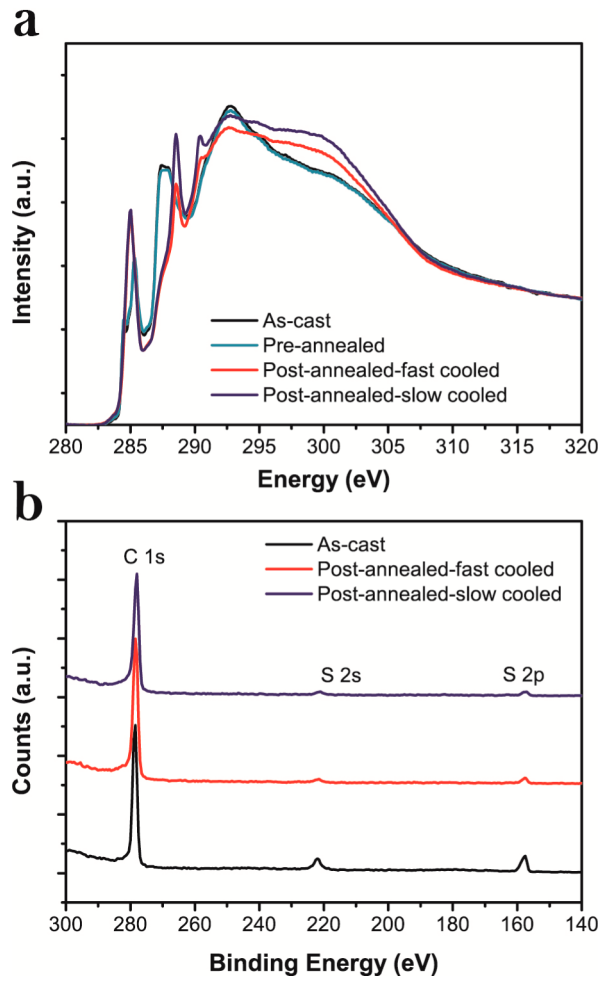

Figure 7. (a) NEXAFS spectra of P3HT/PCBM blend. (b) XPS spectra of P3HT/PCBM blend.

taken at the incidence angle of 55° to mitigate orientational effects. The peaks below 286 eV are related to the resonant transition of a carbon 1s electron into a π^* orbital. The peak at 284.5 eV corresponds to the resonant transition C 1s → π^* of PCBM while the peak at 285.3 corresponds to P3HT; see Figure S3 for the pure spectra. The fraction of P3HT and PCBM were fit as the linear combination of the pristine P3HT and PCBM spectra. The fitting details are presented in Table 3. For the as-cast and preannealed films, there is a P3HT-enriched capping layer observed at the polymer−air interface, consistent with previous studies.[25,34,44] The top ∼3 nm (measured by TEY) of the as-cast, preannealed film contains 14.8 wt % PCBM and 20.6 wt % PCBM, respectively.

In addition, angle-resolved NEXAFS spectra are used to determine the average orientation of P3HT at the air/polymer interface. The intensity of the resonant transition (C 1s → π^*

DOI: 10.1021/acsami.5b03095
ACS Appl. Mater. Interfaces 2015, 7, 14026−14034

Table 3. Fitted Chemical Composition at the Top Surface

		NEXAFS		XPS	
	cooling rates	P3HT (%)	PCBM (%)	P3HT (%)	PCBM (%)
as-cast		85.2	14.8	84.9	15.1
preannealed		79.4	20.6		
postannealed	fast			24.2	75.8
postannealed	slow			22.1	77.9

or C 1s → σ^*) is dependent on the overlap of the electric field vector of the X-ray beam with the corresponding transition dipole moment (TDM).[45,46] When the electric field of synchrotron light is aligned with the TDM of C 1s → π^*, X-rays energy corresponding to that transition are strongly absorbed. As shown in Figure S4, significant dichroism is observed in the resonant transition C 1s → π^* of P3HT (285.3 eV). The strongest X-ray absorption is detected when the X-ray beam is perpendicular to the substrate (the electrical field vector of the X-ray beam parallel to the substrate), indicating an edge-on orientation of P3HT at this interface. As a larger dichroism of the P3HT π^* manifold is observed in the preannealed blend, P3HT shows an increased edge-on configuration after preannealing compared with as-casted film.

The NEXAFS spectra of postannealed films are also shown in Figure 7a. However, because of the degradation of PCBM during the thermal evaporation of Al, a change in the NEXAFS spectra of PCBM has been observed.[47,48] Detailed studies to identify the degradation of PCBM are ongoing. The PCBM C 1s → π^* transition shift means that the NEXAFS spectra of the blend cannot be easily fit to pristine P3HT and PCBM spectra. For this reason, XPS, a complementary technique, has been used to measure the atomic composition of postannealed films, to obtain a similar surface composition measurement. Figure 7b shows XPS of the as-cast and postannealed films with different cooling rates over the binding energy range from 300 to 140 eV, covering the C 1s, S 2s, and S 2p peaks. The chemical composition is calculated from the carbon−sulfur atomic ratio. P3HT contains sulfur, while PCBM does not. The carbon−sulfur atomic ratio is observed to decrease upon postannealing, indicating the diffusion of PCBM toward the polymer/Al interface. From the observed ratios, a surface concentration of 75.8 wt % is found for the postannealed, fast-cooled sample while a surface concentration of 77.9 wt % is found for the postannealed, slow-cooled film. Both of these values are significantly higher than that observed for the as-cast sample (15.1 wt %), indicating a significant enrichment of the PCBM at the blend/Al interface, which aids efficient electron collection.[25,31]

Water contact angle measurements also confirm that P3HT remains at the top of the film in the as-cast and preannealed samples, while PCBM diffuses toward the blend/Al interface in the postannealed films; see Figure 8. The pristine P3HT and PCBM films exhibit water contact angles of 105.8° and 85.8°, respectively (shown in Figure S5). The water contact angle of the preannealed blend shows a value of 106.2°, similar to that of the pristine P3HT, confirming the top surface of the blend is dominated by P3HT. Preannealing shows a negligible effect on the surface energy of the blend, retaining this P3HT capping layer. Significant changes are seen with the postannealed film. The water contact angle of postannealed films with fast- and slow-cooling rates decrease to 68.6° and 63.8°, respectively, close to the water contact angle of postannealed PCBM

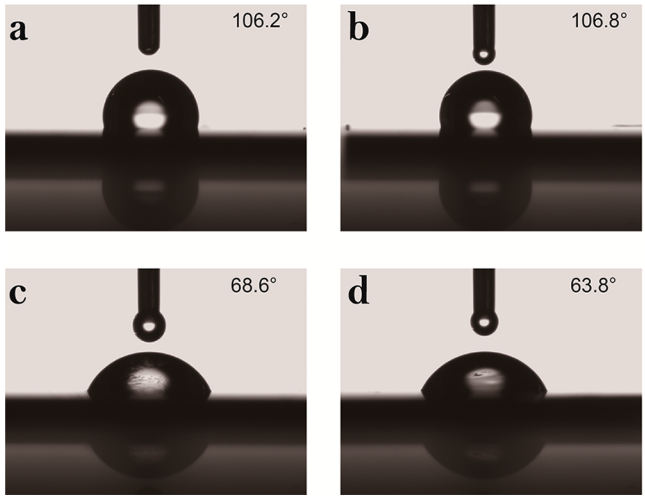

Figure 8. Water contact angle measurements of (a) as-cast blend, (b) preannealed blend, (c) postannealed blend with fast-cooling rate, and (d) postannealed blend with slow-cooling rate.

(57.8°). Enhanced diffusion of PCBM to the interface is observed in the slow-cooled blend from the lower water contact angle. This result is consistent with the NEXAFS and XPS results, indicating that postannealing results in PCBM diffusion to the blend/Al interface, which is enhanced by a slow-cooling rate.

We further investigate the effect of cooling rate on inverted devices as it is increasingly recognized that the inverted architecture exhibits a higher efficiency and better stability.[49] In the inverted structure, polyethylenimine ethoxylate is used to lower the work function of ITO via the formation of a strong dipole layer, which facilitates the electron collection from the ITO side.[50] The photovoltaic performance of inverted P3HT/PCBM solar cells with different thermal treatments is shown in Figure 9a and detailed parameters are summarized in Table 4. The as-cast solar cells yield an average efficiency of 1.95%, a short-circuit current of 5.01 mA/cm^2, an open-circuit current of 0.66 V, and a fill factor of 0.59. Postannealing is detrimental to the device performance; although postannealing shows an increase in short-circuit current to 8.69 mA/cm^2, the efficiency dramatically decreases to 0.95% due to the poor fill factor (0.36). In contrast to conventional architecture devices, a high efficiency is achieved by preannealing these films. The efficiency of preannealed inverted devices increases to 3.64% with the fast-cooling rate, 3.87% for the medium-cooling rate, and 4.15% with the slow-cooling rate, respectively. Compared with a fast-cooled device, the slow-cooled film exhibits higher J_{sc} (10.4 mA/cm^2) and FF (0.67). The integrated EQE shows trends similar to the short-circuit current; see Figure 9b.

The poor efficiency of the postannealed, inverted-architecture devices can be explained by PCBM diffusion toward the blend/MoO_3 interface, the same process which explains increased performance in traditional architecture devices in which PCBM enrichment of the electrode interface is beneficial. Figure 10 shows NEXAFS spectra collected from a postannealed film coated with 2 nm MoO_3. Although the NEXAFS spectrum of the blend is difficult to quantitatively to fit with NEXAFS spectra of pristine P3HT and PCBM due to 2 nm MoO_3 at the top of film, it is clear that a significant increase in the intensity of the peak located at 284.5 eV, which is attributed to a PCBM π^* peak, has been observed, while the

DOI: 10.1021/acsami.5b03095
ACS Appl. Mater. Interfaces 2015, 7, 14026−14034

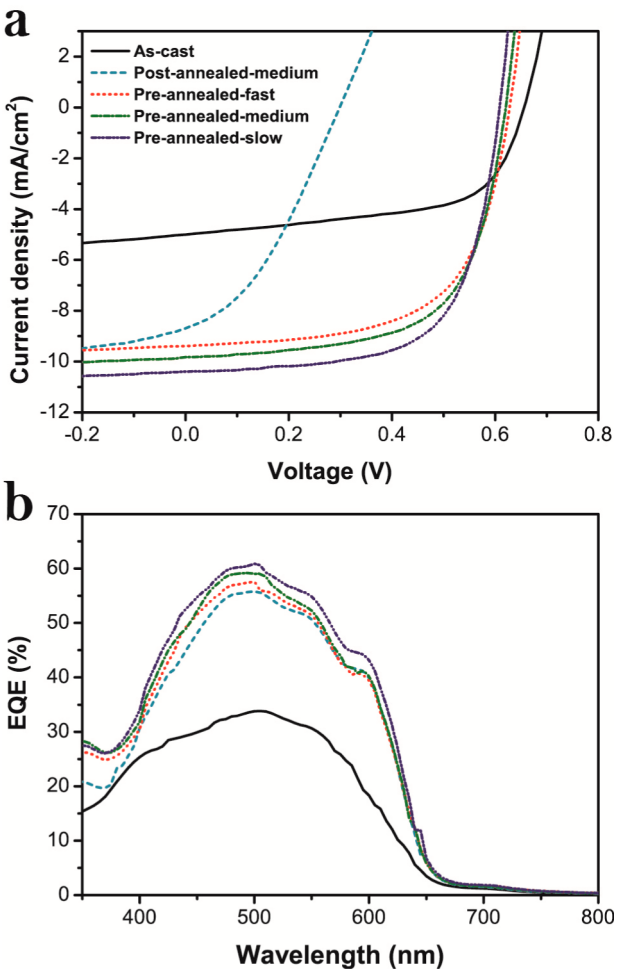

Figure 9. Device performance of inverted P3HT:PCBM solar cells with different cooling rates. (a) Current density versus voltage curve under AM 1.5 G illumination. (b) External quantum efficiency spectra.

Table 4. Photovoltaic Performance of Inverted P3HT/PCBM Solar Cells

	cooling rates	V_{oc} (V)	J_{sc} (mA/cm^2)	FF	efficiency (%)
as-cast		0.66	5.01	0.59	1.95 (±0.11)
preannealed	fast-cooled	0.63	9.40	0.61	3.64 (±0.14)
preannealed	medium-cooled	0.62	9.83	0.63	3.87 (±0.17)
preannealed	slow-cooled	0.6	10.40	0.67	4.15 (±0.19)
postannealed	medium-cooled	0.30	8.69	0.36	0.95 (±0.24)

intensity of the peak located at 285.3 eV, which is related to P3HT π^* manifold, becomes weaker. Thus, the blend/electrode interface is enriched with PCBM after postannealing, hindering the hole collection from MoO_3. The increased concentration of the wrong phase at the top interface in the postannealed inverted device is directly linked to the poorer device performance.

The combination of various advanced techniques provides a comprehensive picture of how the microstructure of the blend changes upon both preannealing and postannealing with the different cooling rates and its relation to device performance. The as-cast polymer exhibits an edge-on dominated configuration with relatively low crystallinity. During the thermal

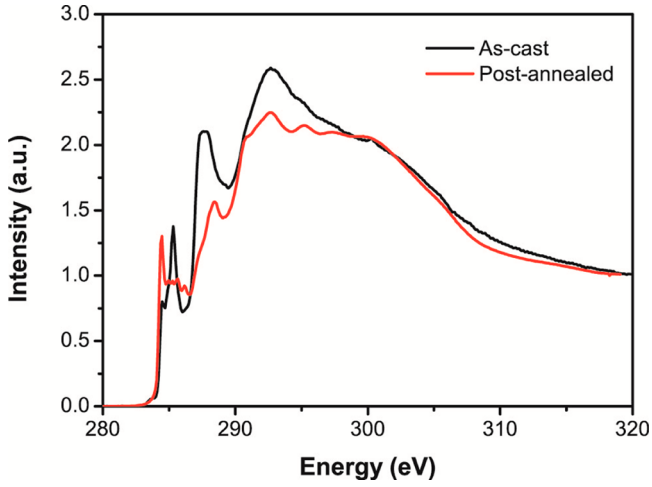

Figure 10. NEXAFS spectrum of a P3HT/PCBM blend postannealed with MoO_3 compared to that of an as-cast sample.

annealing process, the reorganization of P3HT has led to an increased crystallite size in both of out-of-plane and in-plane directions. In the conventional device structure, an efficiency increase from 0.82% for the as-cast device to 1.94% for the preannealed device (medium-cooling rate) and 3.44% for the postannealed device (medium-cooling rate) was seen. In addition, the effects of different cooling rates were also investigated during the thermal annealing treatment. From the GIWAXS results, it is clear that a slow-cooling rate facilitates the polymer reorganization into a face-on configuration rather than an edge-on configuration. The larger coherence length of face-on crystallites has been shown in the slow-cooled blend. Because of the short hopping distance, the hole transport rate along the $\pi-\pi$ stacking direction is faster than that along the (100) direction.[51] A more face-on orientation of P3HT is thought to be beneficial for improving the hole mobility, which is a crucial issue in charge transport for balanced charges after exciton separation. Furthermore, in the postannealed films, we also found that the slow-cooling rate is of importance for the formation of a narrow orientation distribution of the OOP (100) peak. The higher proportion of face-on P3HT crystallites and narrower orientation distribution of crystallites are the reason why the device performance experienced a systematical improvement from fast-cooled to slow-cooled.

Moreover, as-cast blends were found to exhibit a P3HT capping layer on the top surface, consistent with previous studies.[34] Preannealing without a top Al electrode results in a similar surface composition. In contrast, postannealing induces PCBM migration toward the top surface of the BHJ films in both conventional and inverted structure. This vertical redistribution after postannealing is favorable for the conventional structure because of the electron collection from the top electrode. In this morphology, the electrons are efficiently collected by the Al electrode through the percolation pathways of PCBM with reduced charge recombination. In addition, the slightly higher concentration of PCBM at the top surface has been observed in the slow-cooled film, which also contributes to the better device performance. Similar PCBM migration has also been observed at the MoO_3 interface in the postannealed inverted structure. The significant amount of "wrong" materials at this interface is detrimental to the device performance. The efficiency of the inverted device experienced a dramatic drop

DOI: 10.1021/acsami.5b03095
ACS Appl. Mater. Interfaces 2015, 7, 14026−14034

from 1.95% to 0.95%. Therefore, the preannealed device with a P3HT capping layer at the top surface exhibits better efficiency (3.87%, in medium-cooled sample) than the postannealed device (0.95%, in medium-cooled sample).

CONCLUSION

We have presented an in-depth study of the effects of cooling rate, annealing, and device architecture on the morphology and device performance of P3HT:PCBM solar cells. Although thermal annealing of P3HT/PCBM in the presence of an Al electrode results in a wide orientational distribution of edge-on P3HT crystallites, it increases the face-on component of P3HT crystallites and enriches the top electrode interface with PCBM, with these last two effects playing important roles in improving the overall efficiency of the conventional structure. In contrast, postannealing is detrimental to device performance for the inverted structure, with preannealed inverted devices exhibiting a better photovoltaic performance. Choosing when to anneal the sample based on what enrichment is desired at the top interface is critical to device performance. Although different annealing strategies were employed in the different device structures, in all cases a slow-cooling rate was found to give the best efficiency. We conclude that slow cooling allows an optimized morphology with an increased face-on orientation of P3HT crystallites, a better alignment of P3HT crystallites, and beneficial enrichment of the electrode interface. This comprehensive understanding of morphology and device performance for the different cooling rates is of importance for further improving the device efficiency.

ASSOCIATED CONTENT

Supporting Information

NEXAFS spectra and water contact angle measurement of the pristine P3HT and PCBM; angle-resolved NEXAFS spectra of the blend P3HT/PCBM. The Supporting Information is available free of charge on the ACS Publications website at DOI: 10.1021/acsami.5b03095.

AUTHOR INFORMATION

Corresponding Authors

*E-mail: yibing.cheng@monash.edu.
*E-mail: Christopher.mcneill@monash.edu.

Notes

The authors declare no competing financial interest.

ACKNOWLEDGMENTS

NEXAFS spectroscopy and GIWAXS experiments were performed at soft X-ray and SAXS/WAXS beamlines at the Australian Synchrotron, Melbourne, Victoria, Australia. Support from the Australian Renewable Energy Agency (ARENA) is acknowledged; C.R.M. acknowledges support from the Australian Research Council (FT100100275) and Veski.

REFERENCES

(1) Günes, S.; Neugebauer, H.; Sariciftci, N. S. Conjugated Polymer-Based Organic Solar Cells. *Chem. Rev.* **2007**, *107*, 1324−1338.
(2) Forrest, S. R. The Path to Ubiquitous and Low-Cost Organic Electronic Appliances on Plastic. *Nature* **2004**, *428*, 911−918.
(3) Halls, J. J. M.; Walsh, C. A.; Greenham, N. C.; Marseglia, E. A.; Friend, R. H.; Moratti, S. C.; Holmes, A. B. Efficient Photodiodes from Interpenetrating Polymer Networks. *Nature* **1995**, *376*, 498−500.
(4) Yu, G.; Gao, J.; Hummelen, J. C.; Heeger, A. J. Polymer Photovoltaic Cells: Enhanced Efficiencies via a Network of Internal Donor-Acceptor Heterojunction. *Science* **1995**, *270*, 1789−1791.
(5) He, Z.; Zhong, C.; Su, S.; Xu, M.; Wu, H.; Cao, Y. Enhanced Power-Conversion Efficiency in Polymer Solar Cells Using an Inverted Device Structure. *Nat. Photonics* **2012**, *6*, 591−595.
(6) Liu, Y.; Zhao, J.; Li, Z.; Mu, C.; Ma, W.; Hu, H.; Jiang, K.; Lin, H.; Ade, H.; Yan, H. Aggregation and Morphology Control Enables Multiple Cases of High-Efficiency Polymer Solar Cells. *Nat. Commun.* **2014**, *5*, 5293-1−5293-8.
(7) Huang, W.; Gann, E.; Thomsen, L.; Dong, C.; Cheng, Y.-B.; McNeill, C. R. Unraveling the Morphology of High Efficiency Polymer Solar Cells Based on the Donor Polymer PBDTTT-EFT. *Adv. Energy Mater.* **2015**, *5*, 1401259-1−1401259-11.
(8) Dang, M. T.; Hirsch, L.; Wantz, G.; Wuest, J. D. Controlling the Morphology and Performance of Bulk Heterojunctions in Solar Cells. Lessons Learned from the Benchmark Poly(3-hexylthiophene):[6,6]-Phenyl-C61-butyric Acid Methyl Ester System. *Chem. Rev.* **2013**, *113*, 3734−3765.
(9) McNeill, C. R. Morphology of All-Polymer Solar Cells. *Energy Environ. Sci.* **2012**, *5*, 5653−5667.
(10) Li, G.; Zhu, R.; Yang, Y. Polymer Solar Cells. *Nat. Photonics* **2012**, *6*, 153−161.
(11) Ma, W.; Yang, C.; Gong, X.; Lee, K.; Heeger, A. J. Thermally Stable, Efficient Polymer Solar Cells with Nanoscale Control of The Interpenetrating Network Morphology. *Adv. Funct. Mater.* **2005**, *15*, 1617−1622.
(12) Erb, T.; Zhokhavets, U.; Gobsch, G.; Raleva, S.; Stühn, B.; Schilinsky, P.; Waldauf, C.; Brabec, C. J. Correlation Between Structural and Optical Properties of Composite Polymer/Fullerene Films for Organic Solar Cells. *Adv. Funct. Mater.* **2005**, *15*, 1193−1196.
(13) Yang, X.; Loos, J.; Veenstra, S. C.; Verhees, W. J. H.; Wienk, M. M.; Kroon, J. M.; Michels, M. A. J.; Janssen, R. A. J. Nanoscale Morphology of High-Performance Polymer Solar Cells. *Nano Lett.* **2005**, *5*, 579−583.
(14) McNeill, C. R.; Halls, J. J. M.; Wilson, R.; Whiting, G. L.; Berkebile, S.; Ramsey, M. G.; Friend, R. H.; Greenham, N. C. Efficient Polythiophene/Polyfluorene Copolymer Bulk Heterojunction Photovoltaic Devices: Device Physics and Annealing Effects. *Adv. Funct. Mater.* **2008**, *18*, 2309−2321.
(15) Li, G.; Shrotriya, V.; Huang, J.; Yao, Y.; Moriarty, T.; Emery, K.; Yang, Y. High-Efficiency Solution Processable Polymer Photovoltaic Cells by Self-Organization of Polymer Blends. *Nat. Mater.* **2005**, *4*, 864−868.
(16) Li, G.; Yao, Y.; Yang, H.; Shrotriya, V.; Yang, G.; Yang, Y. "Solvent Annealing" Effect in Polymer Solar Cells Based on Poly(3-hexylthiophene) and Methanofullerenes. *Adv. Funct. Mater.* **2007**, *17*, 1636−1644.
(17) Shaheen, S. E.; Brabec, C. J.; Sariciftci, N. S. 2.5% Efficient Organic Plastic Organic Cells. *Appl. Phys. Lett.* **2001**, *78*, 841−843.
(18) Lee, J. K.; Ma, W. L.; Brabec, C. J.; Yuen, J.; Moon, J. S.; Kim, J. Y.; Lee, K.; Bazan, G. C.; Heeger, A. J. Processing Additives for Improved Efficiency from Bulk Heterojunction Solar Cells. *J. Am. Chem. Soc.* **2008**, *130*, 3619−3623.
(19) Peet, J.; Heeger, A. J.; Bazan, G. C. Plastic Solar Cells: Self-Assembly of Bulk Heterojunction Nanomaterials by Spontaneous Phase Separation. *Acc. Chem. Res.* **2009**, *42*, 1700−1708.
(20) Liao, H. C.; Ho, C. C.; Chang, C. Y.; Jao, M. H.; Darling, S. B.; Su, W. F. Additives for Morphology Control in High-Efficiency Organic Solar Cells. *Mater. Today* **2013**, *16*, 326−336.
(21) Padinger, F.; Rittberger, R. S.; Sariciftci, N. S. Effects of Postproduction Treatment on Plastic Solar Cells. *Adv. Funct. Mater.* **2003**, *13*, 85−88.
(22) Chirvase, D.; Parisi, J.; Hummelen, J. C.; Dyakonov, V. Influence of Nanomorphology on the Photovoltaic Action of Polymer−Fullerene Composites. *Nanotechnology* **2004**, *15*, 1317−1323.

DOI: 10.1021/acsami.5b03095
ACS Appl. Mater. Interfaces 2015, 7, 14026−14034

(23) Verploegen, E.; Mondal, R.; Bettinger, C. J.; Sok, S.; Toney, M. F.; Bao, Z. Effects of Thermal Annealing Upon the Morphology of Polymer−Fullerene Blends. *Adv. Funct. Mater.* **2010**, *20*, 3519−3529.
(24) Agostinelli, T.; Lilliu, S.; Labram, J. G.; Campoy-Quiles, M.; Hampton, M.; Pires, E.; Rawle, J.; Bikondoa, O.; Bradley, D. D. C.; Anthopoulos, T. D.; Nelson, J.; Macdonald, J. E. Real-Time Investigation of Crystallization and Phase-Segregation Dynamics in P3HT:PCBM Solar Cells During Thermal Annealing. *Adv. Funct. Mater.* **2011**, *21*, 1701−1708.
(25) Chen, D.; Nakahara, A.; Wei, D.; Nordlund, D.; Russell, T. P. P3HT/PCBM Bulk Heterojunction Organic Photovoltaics: Correlating Efficiency and Morphology. *Nano Lett.* **2010**, *11*, 561−567.
(26) Collins, B. A.; Gann, E.; Guignard, L.; He, X.; McNeill, C. R.; Ade, H. Molecular Miscibility of Polymer−Fullerene Blends. *J. Phys. Chem. Lett.* **2010**, *1*, 3160−3166.
(27) Brabec, C. J.; Heeney, M.; McCulloch, I.; Nelson, J. Influence of Blend Microstructure on Bulk Heterojunction Organic Photovoltaic Performance. *Chem. Soc. Rev.* **2011**, *40*, 1185−1199.
(28) Li, G.; Shrotriya, V.; Yao, Y.; Yang, Y. Investigation of Annealing Effects and Film Thickness Dependence of Polymer Solar Cells Based on Poly(3-hexylthiophene). *J. Appl. Phys.* **2005**, *98*, 043704-1−043704-5.
(29) Marsh, R. A.; Hodgkiss, J. M.; Albert-Seifried, S.; Friend, R. H. Effect of Annealing on P3HT:PCBM Charge Transfer and Nanoscale Morphology Probed by Ultrafast Spectroscopy. *Nano Lett.* **2010**, *10*, 923−930.
(30) Bavel, S. S. v.; Sourty, E.; With, G. d.; Loos, J. Three-Dimensional Nanoscale Organization of Bulk Heterojunction Polymer Solar Cells. *Nano Lett.* **2008**, *9*, 507−513.
(31) Campoy-Quiles, M.; Ferenczi, T.; Agostinelli, T.; Etchegoin, P. G.; Kim, Y.; Anthopoulos, T. D.; Stavrinou, P. N.; Bradley, D. D. C.; Nelson, J. Morphology Evolution via Self-organization and Lateral and Vertical Diffusion in Polymer:Fullerene Solar Cell Blends. *Nat. Mater.* **2008**, *7*, 158−164.
(32) Rivnay, J.; Steyrleuthner, R.; Jimison, L. H.; Casadei, A.; Chen, Z.; Toney, M. F.; Facchetti, A.; Neher, D.; Salleo, A. Drastic Control of Texture in a High Performance n-Type Polymeric Semiconductor and Implications for Charge Transport. *Macromolecules* **2011**, *44*, 5246−5255.
(33) Yu, L.; Li, C.; Li, Q.; Wang, F.; Lin, J.; Liu, J.; Hu, S.; Zheng, H.; Tan, Z. Performance improvement of conventional and inverted polymer solar cells with hydrophobic fluoropolymer as nonvolatile processing additive. *Org. Electron.* **2015**, *23*, 99−104.
(34) Xue, B.; Vaughan, B.; Poh, C.-H.; Burke, K. B.; Thomsen, L.; Stapleton, A.; Zhou, X.; Bryant, G. W.; Belcher, W.; Dastoor, P. C. Vertical Stratification and Interfacial Structure in P3HT:PCBM Organic Solar Cells. *J. Phys. Chem. C* **2010**, *114*, 15797−15805.
(35) Kirby, N. M.; Mudie, S. T.; Hawley, A. M.; Cookson, D. J.; Mertens, H. D. T.; Cowieson, N.; Samardzic-Boban, V. A Low-Background-Intensity Focusing Small-Angle X-ray Scattering Undulator Beamline. *J. Appl. Crystallogr.* **2013**, *46*, 1670−1680.
(36) Ilavsky, J. Nika: Software for Two-Dimensional Data Reduction. *J. Appl. Crystallogr.* **2012**, *45*, 324−328.
(37) Gann, E.; Gao, X.; Di, C.-a.; McNeill, C. R. Phase Transitions and Anisotropic Thermal Expansion in High Mobility Core-expanded Naphthalene Diimide Thin Film Transistors. *Adv. Funct. Mater.* **2014**, *24*, 7211−7220.
(38) Cowie, B. C. C.; Tadich, A.; Thomsen, L. The Current Performance of the Wide Range (90−2500 eV) Soft X-ray Beamline at the Australian Synchrotron. *AIP Conf. Proc.* **2010**, *1234*, 307−310.
(39) Gann, E.; McNeill, C. R.; Szumilo, M.; Sirringhaus, H.; Sommer, M.; Maniam, S.; Langford, S. J.; Thomsen, L. Near-Edge X-ray Absorption Fine-Structure Spectroscopy of Naphthalene Diimide-Thiophene Co-Polymers. *J. Chem. Phys.* **2014**, *140*, 164710.
(40) Schuettfort, T.; Thomsen, L.; McNeill, C. R. Observation of a Distinct Surface Molecular Orientation in Films of a High Mobility Conjugated Polymer. *J. Am. Chem. Soc.* **2013**, *135*, 1092−1101.
(41) Clark, J.; Silva, C.; Friend, R. H.; Spano, F. C. Role of Intermolecular Coupling in the Photophysics of Disordered Organic Semiconductors: Aggregate Emission in Regioregular Polythiophene. *Phys. Rev. Lett.* **2007**, *98*, 206406.
(42) Zhokhavets, U.; Erb, T.; Gobsch, G.; Al-Ibrahim, M.; Ambacher, O. Relation Between Absorption and Crystallinity of Poly(3-hexylthiophene)/Fullerene Films for Plastic Solar Cells. *Chem. Phys. Lett.* **2006**, *418*, 347−350.
(43) Treat, N. D.; Shuttle, C. G.; Toney, M. F.; Hawker, C. J.; Chabinyc, M. L. In situ measurement of power conversion efficiency and molecular ordering during thermal annealing in P3HT:PCBM bulk heterojunction solar cells. *J. Mater. Chem.* **2011**, *21*, 15224−15231.
(44) Tillack, A. F.; Noone, K. M.; MacLeod, B. A.; Nordlund, D.; Nagle, K. P.; Bradley, J. A.; Hau, S. K.; Yip, H.-L.; Jen, A. K. Y.; Seidler, G. T.; Ginger, D. S. Surface Characterization of Polythiophene:Fullerene Blends on Different Electrodes Using Near Edge X-ray Absorption Fine Structure. *ACS Appl. Mater. Interfaces* **2011**, *3*, 726−732.
(45) Hahner, G. Near Edge X-ray Absorption Fine Structure Spectroscopy as a Tool to Probe Electronic and Structural Properties of Thin Organic Films and Liquids. *Chem. Soc. Rev.* **2006**, *35*, 1244−1255.
(46) McNeill, C. R.; Ade, H. Soft X-ray Characterisation of Organic Semiconductor Films. *J. Mater. Chem. C* **2013**, *1*, 187−201.
(47) Matz, D. L.; Ratcliff, E. L.; Meyer, J.; Kahn, A.; Pemberton, J. E. Deciphering the Metal-C60 Interface in Optoelectronic Devices: Evidence for C60 Reduction by Vapor Deposited Al. *ACS Appl. Mater. Interfaces* **2013**, *5*, 6001−6008.
(48) Mauger, S. A.; Chang, L.; Friedrich, S.; Rochester, C. W.; Huang, D. M.; Wang, P.; Moulé, A. J. Self-Assembly of Selective Interfaces in Organic Photovoltaics. *Adv. Funct. Mater.* **2013**, *23*, 1935−1946.
(49) Tan, M. J.; Zhong, S.; Li, J.; Chen, Z.; Chen, W. Air-Stable Efficient Inverted Polymer Solar Cells Using Solution-Processed Nanocrystalline ZnO Interfacial Layer. *ACS Appl. Mater. Interfaces* **2013**, *5*, 4696−4701.
(50) Zhou, Y.; Fuentes-Hernandez, C.; Shim, J.; Meyer, J.; Giordano, A. J.; Li, H.; Winget, P.; Papadopoulos, T.; Cheun, H.; Kim, J.; Fenoll, M.; Dindar, A.; Haske, W.; Najafabadi, E.; Khan, T. M.; Sojoudi, H.; Barlow, S.; Graham, S.; Brédas, J.-L.; Marder, S. R.; Kahn, A.; Kippelen, B. A Universal Method to Produce Low-Work Function Electrodes for Organic Electronics. *Science* **2012**, *336*, 327−332.
(51) Sirringhaus, H.; Brown, P. J.; Friend, R. H.; Nielsen, M. M.; Bechgaard, K.; Langeveld-Voss, B. M. W.; Spiering, A. J. H.; Janssen, R. A. J.; Meijer, E. W.; Herwig, P.; de Leeuw, D. M. Two-Dimensional Charge Transport in Self-Organized, High-Mobility Conjugated Polymers. *Nature* **1999**, *401*, 685−688.

DOI: 10.1021/acsami.5b03095
ACS Appl. Mater. Interfaces 2015, 7, 14026−14034